

# Structure and Dynamics of Ca<sup>2+</sup>-Binding Domain 1 of the Na<sup>+</sup>/Ca<sup>2+</sup> Exchanger in the Presence and in the Absence of Ca<sup>2+</sup>

Eric Johnson<sup>1</sup>, Lei Bruschiweiler-Li<sup>1</sup>, Scott A. Showalter<sup>1</sup>, Geerten W. Vuister<sup>2</sup>, Fengli Zhang<sup>1</sup> and Rafael Brüschiweiler<sup>1\*</sup>

<sup>1</sup>Department of Chemistry and Biochemistry and National High Magnetic Field Laboratory, Florida State University, Tallahassee, FL 32306, USA

<sup>2</sup>Protein Biophysics, Institute for Molecules and Materials, Radboud University Nijmegen, Toernooiveld 1, 6525 ED Nijmegen, The Netherlands

Received 19 October 2007;  
received in revised form  
17 January 2008;  
accepted 18 January 2008  
Available online  
30 January 2008

The Na<sup>+</sup>/Ca<sup>2+</sup> exchanger is the major exporter of Ca<sup>2+</sup> across the cell membrane of cardiomyocytes. The activity of the exchanger is regulated by a large intracellular loop that contains two Ca<sup>2+</sup>-binding domains, calcium-binding domain (CBD) 1 and CBD2. CBD1 binds Ca<sup>2+</sup> with much higher affinity than CBD2 and is considered to be the primary Ca<sup>2+</sup> sensor. The effect of Ca<sup>2+</sup> on the structure and dynamics of CBD1 has been characterized by NMR spectroscopy using chemical shifts, residual dipolar couplings, and spin relaxation. Residual dipolar couplings are used in a new way for residue selection in the determination of the anisotropic rotational diffusion tensor from spin relaxation data. The results provide a highly consistent description across these complementary data sets and show that Ca<sup>2+</sup> binding is accompanied by a selective conformational change among the binding site residues. Residues that exhibit a significant conformational change are also sites of altered dynamics. In particular, Ca<sup>2+</sup> binding restricts the mobility of the major acidic segment and affects the dynamics of several nearby binding loops. These observations indicate that Ca<sup>2+</sup> elicits a local transition to a well-ordered coordination geometry in the CBD1-binding site.

© 2008 Elsevier Ltd. All rights reserved.

**Keywords:** Na<sup>+</sup>/Ca<sup>2+</sup> exchanger; Ca<sup>2+</sup>-binding proteins; NMR relaxation; backbone dynamics; residual dipolar couplings

Edited by A. G. Palmer III

## Introduction

Calcium ions (Ca<sup>2+</sup>) act as universal second messengers that regulate many different cellular functions.<sup>1,2</sup> In the heart, for example, an influx of Ca<sup>2+</sup> into the cytosol leads to muscle contraction. In order for the heart to function optimally, the same amount of Ca<sup>2+</sup> that enters the cytosol at the start of the cardiac cycle must be efficiently removed from the cytosol, allowing the heart to relax and refill with blood. Defects in Ca<sup>2+</sup> cycling result in smaller and slower Ca<sup>2+</sup> transients that are characteristic of heart failure.<sup>3</sup> The major exporter of Ca<sup>2+</sup> across the

plasma membrane is the Na<sup>+</sup>/Ca<sup>2+</sup> exchanger (NCX), whose dominant mode of transport is the export of one Ca<sup>2+</sup> for the uptake of three Na<sup>+</sup>.<sup>4–6</sup>

A simplified topology model for the NCX predicts nine transmembrane  $\alpha$ -helices and a large intracellular loop of approximately 500 residues located between helices 5 and 6.<sup>7,8</sup> A more detailed description of the intracellular loop in solution was recently obtained by NMR structure determination of two Ca<sup>2+</sup>-binding domains, calcium-binding domain (CBD) 1 and CBD2, present in the NCX.<sup>9</sup> This study also provided evidence of a third intracellular domain that relays the Ca<sup>2+</sup> signal from the regulatory domains CBD1 and CBD2 to the Ca<sup>2+</sup> transport sites located within the transmembrane segments (Fig. 1a). The structures of Ca<sup>2+</sup>-bound CBD1 and CBD2 both exhibit an immunoglobulin fold whose core consists of two antiparallel  $\beta$ -sheets that form a compact  $\beta$ -sandwich, with a large unstructured loop, the FG loop, connecting strands F and G (Fig. 1b). The structure of CBD1 has also been determined by X-ray crystallography, which revealed

\*Corresponding author. E-mail address: [bruschweiler@magnet.fsu.edu](mailto:bruschweiler@magnet.fsu.edu).

Abbreviations used: NCX, Na<sup>+</sup>/Ca<sup>2+</sup> exchanger; CBD, calcium-binding domain; RDC, residual dipolar coupling; HSQC, heteronuclear single quantum coherence; cNtnc, N-domain of cardiac troponin C.

four bound  $\text{Ca}^{2+}$  coordinated primarily by side-chain carboxylate groups from two acidic segments located in the EF loop (D446–E454) and near the G-strand at the C-terminus (D498–D500).<sup>11</sup> It was previously suggested that the upper half of CBD1 is unstructured in the absence of  $\text{Ca}^{2+}$ , while CBD2 maintains its structural integrity in the  $\text{Ca}^{2+}$ -free (apo) state.<sup>9</sup> A fluorescent resonance energy transfer study in which two fluorophores were linked to

CBD1 indicates that  $\text{Ca}^{2+}$  binding elicits a conformational change in this domain.<sup>12</sup> Based on these structural observations, together with the fact that CBD1 exhibits a higher affinity for  $\text{Ca}^{2+}$  than does CBD2,<sup>9</sup> it has been suggested that CBD1 is the primary  $\text{Ca}^{2+}$  sensor in the NCX.

There is currently no structure available for the apo state of CBD1. X-ray crystallographic studies of  $\text{Ca}^{2+}$ -binding proteins are often hindered by an inability to obtain suitable crystals in both the presence and the absence of  $\text{Ca}^{2+}$ . NMR spectroscopic studies are not limited in this regard as they are performed in solution where the  $\text{Ca}^{2+}$  concentration can be freely adjusted. This capability has enabled several comparison studies between structural data from  $\text{Ca}^{2+}$ -bound states and apo states.<sup>13–30</sup> In the case of CBD1, the quantitative comparison between the two states has been deemed challenging due to a significant amount of disorder attributed to the apo state.<sup>9</sup> A detailed comparison of the two states, however, has been achieved in the current study through the use of multiple NMR observables. NMR chemical shifts and residual dipolar couplings (RDCs) identify sites where the apo structure differs significantly from that of the  $\text{Ca}^{2+}$ -bound state. In addition, NMR relaxation methods provide a detailed characterization of the protein's conformational dynamics in the two states.<sup>31–33</sup> If  $\text{Ca}^{2+}$  binding does in fact elicit a disorder–order transition, then the dynamics amplitudes of the  $\text{Ca}^{2+}$ -bound state should be significantly reduced compared to the apo state.

Backbone NMR relaxation methods have been successfully applied to several other  $\text{Ca}^{2+}$ -binding proteins.<sup>34–48</sup> Many of these protein systems belong to the EF-hand family. The EF-hand motif is represented in some of the proteins most extensively studied by NMR, including calbindin  $\text{D}_{9k}$ , calmodulin, and the regulatory domain of troponin C.<sup>49–52</sup> These proteins exhibit a helix–loop–helix motif whose fold and binding geometry are significantly different from those of CBD1. The  $\beta$ -sandwich and binding loops of CBD1 are more closely associated with the  $\text{C}_2$ -domain family, which represents another common  $\text{Ca}^{2+}$ -binding motif.<sup>53,54</sup>  $\text{C}_2$  domains often play significant roles in signal transduction and membrane traffic.<sup>55</sup> Although the  $\text{C}_2$  domain is present in several published structures,<sup>27,56–58</sup> little

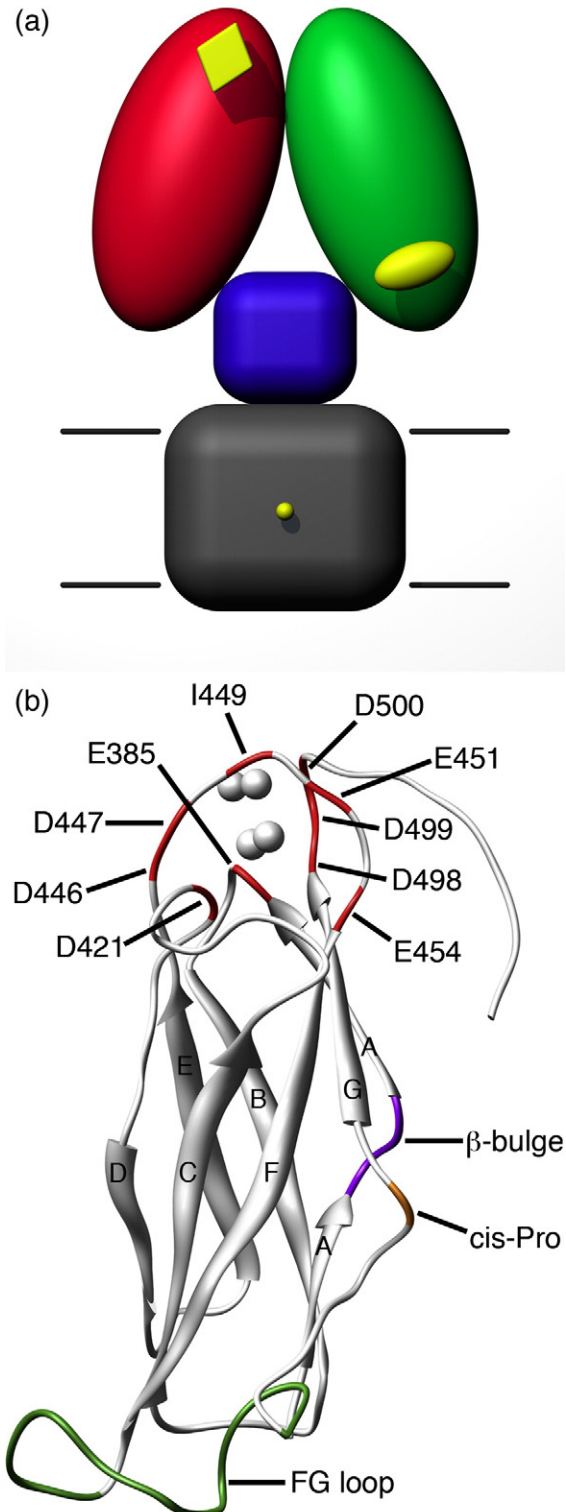


**Fig. 1.** (a) Model of the intact exchanger composed of CBD1 (red), CBD2 (green), a third intracellular domain (blue), and the transmembrane segments (gray).  $\text{Ca}^{2+}$ -binding sites are represented in yellow. (b) Representative member (lowest energy) of the NMR structural ensemble (2FWS). The positions of the four  $\text{Ca}^{2+}$  (represented as spheres) are derived from the corresponding crystal structure (2DPK). Selected structural elements are labeled and color-coded as follows: (1) residues that contribute  $\text{Ca}^{2+}$ -binding ligands (red); (2)  $\beta$ -bulge (purple); (3) *cis*-Pro (orange); and (4) FG loop (green).  $\beta$ -Strands are labeled A–G. Molecular graphics were produced using the UCSF Chimera package (supported by National Institutes of Health grant P41 RR-01081).<sup>10</sup>

is known about the effects of  $\text{Ca}^{2+}$  on the fast time-scale dynamics of this domain. The present study aims to provide a quantitative description of the structure and dynamics of this common  $\text{Ca}^{2+}$ -binding motif, with the goal to better understand its binding mechanism at atomic detail.

## Results and Discussion

### Analytical ultracentrifugation

Potential partial oligomerization of both the  $\text{Ca}^{2+}$ -bound state and the apo state of CBD1 was assessed by analytical ultracentrifugation at 400  $\mu\text{M}$  (i.e., at NMR concentrations). The results show that both states exist as single species whose molecular weights are consistent with that of the monomer (see Supplementary Materials). These findings are also corroborated by  $^{15}\text{N}$  relaxation data (vide infra).

### Chemical shift analysis

A superposition of the  $[^1\text{H}, ^{15}\text{N}]$  heteronuclear single quantum coherence (HSQC) spectra at 800 MHz for CBD1 in the  $\text{Ca}^{2+}$ -bound state (red) and in the apo state (blue) is represented in Fig. 2. Both states exhibit high-quality spectra with good peak dispersion for a protein of this size (15.2 kDa). The  $[^1\text{H}, ^{15}\text{N}]$  HSQC spectra indicate that only 22 of the 139 total residues are missing or overlapping in both states. One of the overlapping residues (D499) directly participates in  $\text{Ca}^{2+}$  binding (i.e., it contributes a  $\text{Ca}^{2+}$ -binding ligand). An additional five residues are overlapped in the  $\text{Ca}^{2+}$ -bound state only, while an additional 12 residues, including residues E454, D498, and D500 of the acidic segments, are overlapped in the apo state only.

Resonance assignments for the  $\text{Ca}^{2+}$ -bound state of CBD1 were previously reported by Hilge *et al.*<sup>9</sup> Resonance assignments for the apo state were de-

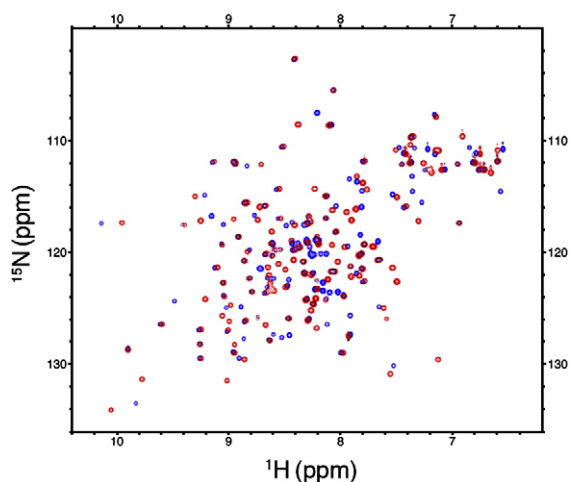


**Fig. 2.** Overlay of the  $[^1\text{H}, ^{15}\text{N}]$  HSQC spectra. The  $\text{Ca}^{2+}$ -bound state and the apo state are represented in red and blue, respectively.

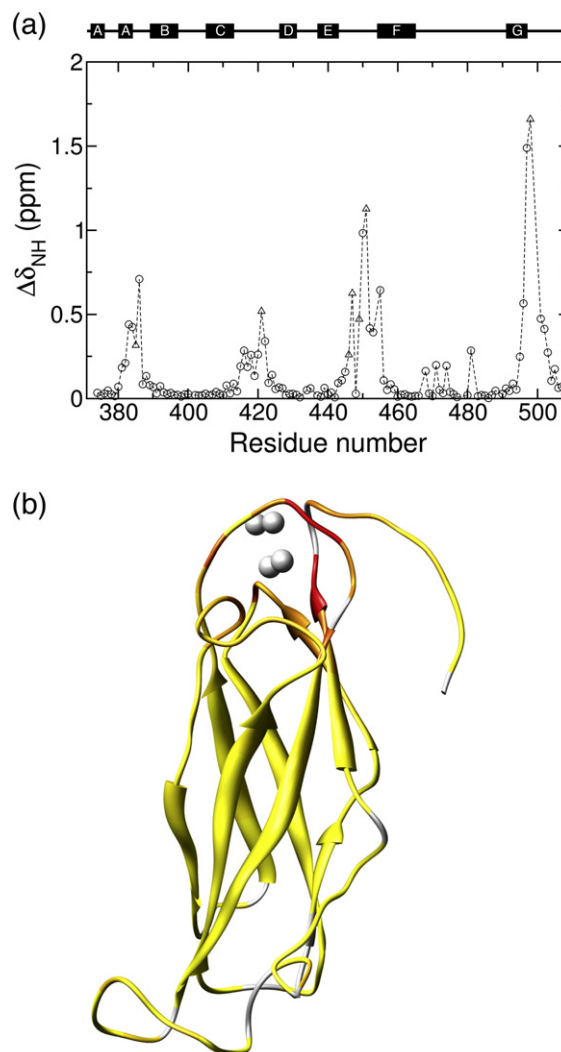


**Fig. 3.** (a) Plot of the amide chemical shift change  $\Delta\delta_{\text{NH}}$  as a function of residue number. Residues that contribute a  $\text{Ca}^{2+}$ -binding ligand are represented by triangles. (b) Structural context for the amide chemical shift change. The color gradient extends from yellow (for  $\Delta\delta_{\text{NH},i}=0$ ) to red (for  $\Delta\delta_{\text{NH},i}\geq 1$ ).

termined in the present study by working at a lower protein concentration and a higher salt concentration, improving the sample stability. The results indicate that many nuclei experience similar structures and surroundings in the  $\text{Ca}^{2+}$ -bound state and the apo state. Residues for which  $\text{Ca}^{2+}$  binding elicits a substantial change in chemical environment are indicated by large values of the amide chemical shift change:

$$\Delta\delta_{\text{NH},i} = \left[ \Delta\delta_{\text{H},i}^2 + (\Delta\delta_{\text{N},i}/5)^2 \right]^{1/2}$$

where  $\Delta\delta_{\text{H},i}$  and  $\Delta\delta_{\text{N},i}$  are the amide  $^1\text{H}$  and  $^{15}\text{N}$  chemical shift differences between the two states for residue  $i$ .<sup>59</sup> In Fig. 3a, the amide chemical shift change is plotted as a function of residue number. Figure 3b maps this same information onto the CBD1 structure using color coding from yellow (for

$\Delta\delta_{\text{NH},i}=0$  ppm) to red (for  $\Delta\delta_{\text{NH},i}\geq 1$  ppm).  $\text{Ca}^{2+}$ -binding residues are represented by triangles in Fig. 3a. The largest amide chemical shift changes cluster in four regions of the protein sequence, each of which contributes one or more  $\text{Ca}^{2+}$ -binding ligands. The acidic segments near residues 450 and 500 exhibit particularly large  $\Delta\delta_{\text{NH},i}$  values across multiple consecutive residues.

### RDC analysis

One-bond backbone  $^{15}\text{N}$ - $^1\text{H}$  RDCs were measured for the  $\text{Ca}^{2+}$ -bound state and the apo state in a liquid crystalline medium containing C12E5/hexanol.<sup>60–65</sup> The use of a liquid crystalline medium results in weak alignment of the protein molecules with respect to the external magnetic field leading to the observed RDCs. This information provides a set of restraints on bond vector orientations that is commonly used in structure validation studies. The RDCs for both states were fit to the  $\text{Ca}^{2+}$ -bound crystal structure in order to probe for a  $\text{Ca}^{2+}$ -dependent conformational change. Figure 4a and b shows the correlation between the RDCs observed experimentally and the values that are calculated from the CBD1 crystal structure. The red points correspond to residues that were excluded from the calculation of the alignment tensor due to relatively poor agreement with the crystal structure (details provided in the Materials and Methods section).

The level of agreement between the experimental RDC and the calculated RDC is expressed in terms of a  $Q$  value, which depends on the resolution of the available structure. In the present case, the crystal structure was determined at 2.5 Å resolution, which is expected to yield a  $Q$  value of around 0.40.<sup>61</sup> The  $Q$  values for the  $\text{Ca}^{2+}$ -bound state and the apo state are 0.31 and 0.49, respectively, indicating that the RDCs for the core domain of both states are largely consistent with the crystal structure. The RDCs of the  $\text{Ca}^{2+}$ -bound state are expected to provide a lower  $Q$  value (i.e., better agreement) due to the fact that the crystal structure corresponds to the  $\text{Ca}^{2+}$ -loaded form. The agreement is still relatively good, however, for the apo state, suggesting only limited changes in the core  $\beta$ -sandwich structure. Consistent with this finding is the similarity of the alignment tensors for the two states. The axial components are 14.1 and 15.4 Hz, while the rhombicities amount to 0.18 and 0.17 for the  $\text{Ca}^{2+}$ -bound state and the apo state, respectively (for definitions of these quantities, see Meiler *et al.*<sup>66</sup>). There are clear site-specific differences between the two states that are apparent in a correlation plot of the experimental RDCs (Fig. 4c). Residues 449, 450, 451, and 452 exhibit particularly large differences. These residues are located in the middle of the major acidic segment that includes 5 of the 10 residues that contribute  $\text{Ca}^{2+}$ -binding ligands. The absolute value of the N–H RDC for each residue in this segment is uniformly higher in the  $\text{Ca}^{2+}$ -bound state than in the apo state (Fig. 4c), which is consistent with the presence of significant motional averaging of these RDCs.<sup>66</sup> Together with

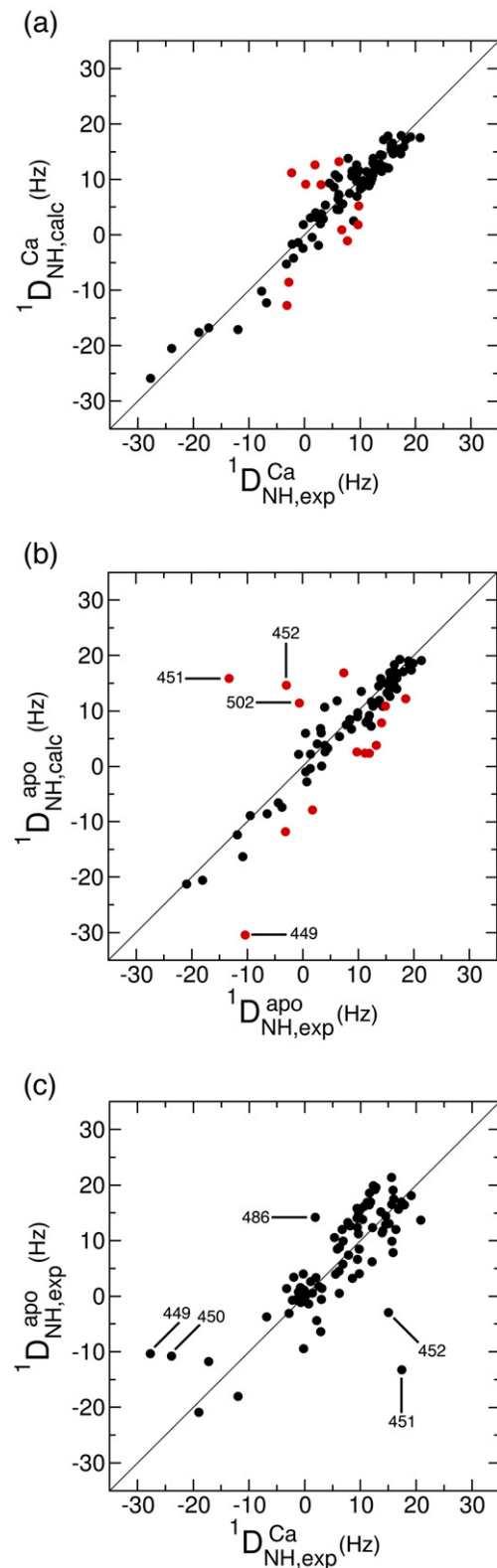


**Fig. 4.** Correlation plot between the experimental and the back-calculated one-bond  $^{15}\text{N}$ - $^1\text{H}$  RDCs for the  $\text{Ca}^{2+}$ -bound state (a) and the apo state (b). In both cases, the experimental data were fit to the  $\text{Ca}^{2+}$ -bound crystal structure (2DPK). Residues that were excluded from the alignment tensor calculation are represented in red. The correlation between the experimental RDCs for both states is shown in (c).

the large chemical shift differences observed in the region centered near residue 450, these observations indicate that  $\text{Ca}^{2+}$  binding requires a localized conformational and dynamic change involving several of the binding site residues.

### $^{15}\text{N}$ relaxation analysis of overall tumbling motion

$^{15}\text{N}$  NMR relaxation data report on fast time-scale (picosecond to nanosecond) reorientational motions.<sup>31–33</sup> In order to characterize the effects of  $\text{Ca}^{2+}$  binding on the backbone dynamics of CBD1, longitudinal ( $T_1$ ) and transverse ( $T_2$ ) relaxation times, as well as  $\{^1\text{H}\}$ - $^{15}\text{N}$  steady-state nuclear Overhauser effects, were measured both in the presence and in the absence of  $\text{Ca}^{2+}$  (relaxation data provided in Supplementary Materials). The relaxation data were then analyzed using the model-free method of Lipari and Szabo.<sup>67</sup> The Lipari–Szabo method provides a generalized order parameter  $S^2$  and an internal correlation time  $\tau_{\text{int}}$ , which indicate the amplitude and time scale, respectively, of internal motion at a given site. Extraction of meaningful model-free parameters requires the accurate description of the overall rotational diffusion tensor with an average correlation time  $\tau_c$ . This aspect of the analysis is particularly critical in the case of molecules whose tumbling is highly anisotropic, such as CBD1. In order to optimize the rotational diffusion tensor,<sup>68</sup> a set of core residues that satisfied the following criteria was selected: (1) good RDC agreement with the crystal structure; (2) no signs of conformational exchange; and (3) small  $\tau_{\text{int}}$  values (details provided in the Materials and Methods section). The cylindrical shape of the three-dimensional structure of CBD1 suggests that a prolate, axially symmetric ellipsoid applies in good approximation for this molecule.

When using the crystal structure as a reference, the combination of the Lipari–Szabo approach with Woessner equations gives  $\tau_c$  values of  $12.30 \pm 0.01$  and  $11.03 \pm 0.02$  ns and  $D_{\parallel}/D_{\perp}$  ratios of  $2.10 \pm 0.02$  and  $1.84 \pm 0.03$  for the  $\text{Ca}^{2+}$ -bound state and the apo state, respectively. Similar values are obtained by the quadric method, which provides an alternative route to the global diffusion parameters.<sup>69</sup> Although the quadric method is best suited for diffusion tensors with relatively small anisotropies, it provides results for CBD1 that are remarkably consistent with those of the Woessner method.<sup>70</sup> The quadric method gives  $\tau_c$  values of  $12.57 \pm 0.01$  and  $11.14 \pm 0.02$  ns and  $D_{\parallel}/D_{\perp}$  ratios of  $2.00 \pm 0.01$  and  $1.78 \pm 0.02$  for the  $\text{Ca}^{2+}$ -bound state and the apo state, respectively. The quality of the fits is high, providing additional evidence that the  $\text{Ca}^{2+}$ -bound crystal structure is a reasonable model for the core of both the  $\text{Ca}^{2+}$ -bound state and the apo state. The apo state, however, is slightly more sensitive to the criteria used to select residues for the diffusion tensor optimization, due to the fact that the number of available bond vectors is limited by the lack of a high-resolution apo structure. The present results

demonstrate, however, that the rotational diffusion of CBD1 is slower and more anisotropic in the presence of  $\text{Ca}^{2+}$ , which is likely caused by the structuring of the binding site loops upon  $\text{Ca}^{2+}$  binding. The higher mobility of the  $\text{Ca}^{2+}$ -binding loop of the apo state, on the other hand, renders its effective hydrodynamic volume smaller and its shape more isotropic.

### Flexible regions outside the binding loops

The generalized N–H order parameters  $S^2$  for both states were determined with the Woessner model for anisotropic tumbling and are plotted as a function of residue number in Fig. 5a. The two states

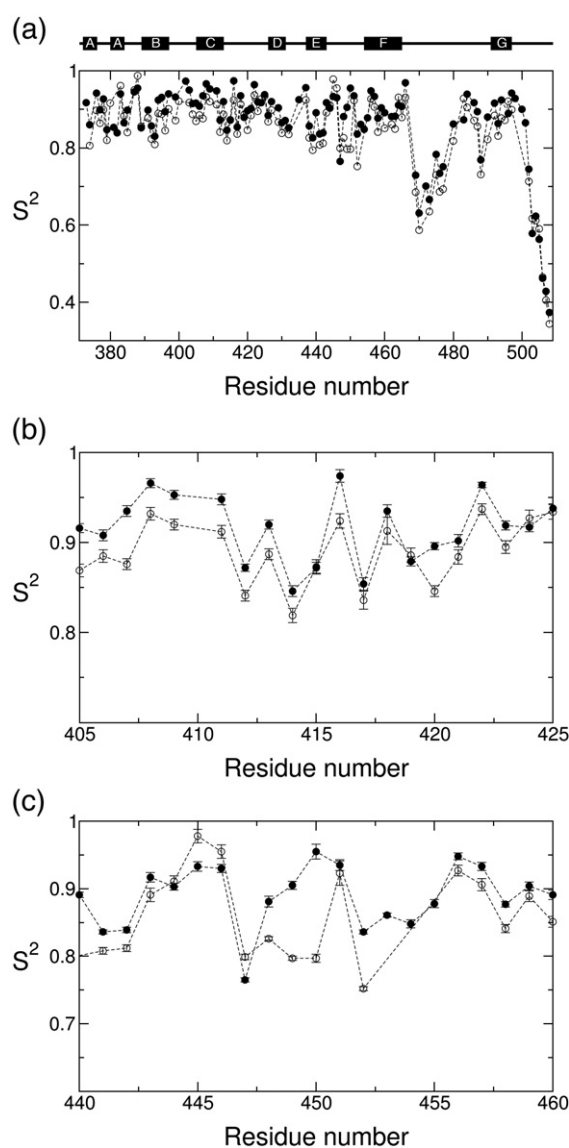


**Fig. 5.** (a) The generalized order parameter  $S^2$  plotted as a function of residue number for the  $\text{Ca}^{2+}$ -bound state (closed circle) and the apo state (open circle). Order parameters for residues near strand C are highlighted in (b), while order parameters for the major acidic segment are highlighted in (c).

exhibit very similar  $S^2$  profiles across large segments of the molecule. There is a consistent trend, however, in which the  $S^2$  values for residues in the core of the domain are slightly higher (around 0.025) in the  $\text{Ca}^{2+}$ -bound state than in the apo state (Fig. 5b). It is considered unlikely that a uniform offset reflects an actual difference in the internal dynamics of the two states. Rather, the  $S^2$  difference is more likely attributed to the aforementioned uncertainty in the apo diffusion tensor. Model calculations confirm that for the majority of bond vector orientations, a small increase in the apparent diffusion tensor anisotropy is reflected in a small systematic increase in the resulting order parameters. Several residues, however, exhibit changes in  $S^2$  that are much larger than this overall effect (vide infra).

The low  $S^2$  values in the FG loop (residues 467–491) and C-terminus indicate that these regions are highly flexible, in agreement with their poor definitions in the NMR structural ensemble and the missing electron density in the crystal structure. It is not yet known if the high mobility at these sites is preserved in the intact exchanger. A model of the intact exchanger suggests that the FG loop and the C-terminus may be subject to additional steric constraints in the NCX that are not present in the isolated domain,<sup>9</sup> suggesting that the  $S^2$  values for these sites might actually be higher in the intact exchanger. Previous studies of other proteins with the immunoglobulin fold indicate that the mobility of the FG loop determines the specificity of binding for various receptors. High mobility is observed in cases where the FG loop binds to multiple receptors, while more restricted dynamics are observed in cases where the FG loop exhibits higher specificity.<sup>71,72</sup> It is presently unknown whether the mobility of the FG loop plays a similar role in CBD1. To address this point, dynamics studies need to be carried out using larger NCX constructs.

In addition to the local minimum in the order parameter profile of the FG loop at Ser470, a second local minimum is found at Ser488. Although this residue is well-defined in the crystal structure, the  $S^2$  values indicate that Ser488 is highly flexible in both states. This observation is consistent with a high level of structural uncertainty in this region, as reflected by the RDCs. Several nearby residues exhibit poor RDC agreement with the crystal structure (residues 483, 486, and 491 in the  $\text{Ca}^{2+}$ -bound state, and residue 486 in the apo state). In addition, superposition of the NMR and crystal structures reveals that the distance between the corresponding  $\text{C}^\alpha$  atoms in the two structures is particularly high in the region ( $>4 \text{ \AA}$  for residues 481, 483, 484, and 485). The relationship between average structure and dynamics is further elucidated by the local sequence context. Ser488 is located near strand G between a glycine and a *cis*-proline. The *cis*-proline at residue 489 induces a protrusion that is commonly observed in immunoglobulin folds.<sup>73</sup> It has been suggested that this structural distortion represents a natural element of negative design.<sup>11,74</sup> Disruption of the outer strand G disfavors the formation of

intermolecular hydrogen bonds, thereby inhibiting aggregation of CBD1 with other  $\beta$ -sheet proteins. The fact that this structural distortion is accompanied by large-amplitude dynamics suggests that both structure and dynamics may serve a protective role. From a thermodynamic perspective, the inability to form stable hydrogen bonds disfavors intermolecular association by increasing the enthalpy change of the process. In addition, edge-to-edge aggregation would restrict the large-amplitude dynamics that are currently observed at Ser488, which would disfavor intermolecular association by decreasing the corresponding entropy change. Such an entropic penalty represents a novel element of negative design, suggesting that evolution may actually employ a dual protective strategy that includes both structural (enthalpic) and dynamic (entropic) effect.

### Dynamics changes in the binding loops

Although the  $\text{Ca}^{2+}$ -bound state and the apo state exhibit similar backbone dynamics across large segments of the molecule, the two states exhibit substantial differences in the dynamics of the major acidic segment (Fig. 5c). Five residues in this segment (D446, D447, I449, E451, and E454) contribute  $\text{Ca}^{2+}$ -binding ligands. Of these five, D447 and I449 are particularly relevant to the current study due to the fact that they coordinate  $\text{Ca}^{2+}$  4 and 3, respectively, via backbone carbonyl oxygens. These backbone-ion interactions are expected to restrict the mobility of the corresponding amide planes, which include the backbone N–H groups of D448 and F450. Immobilization of these residues is reflected by their  $S^2$  values, which are significantly higher in the  $\text{Ca}^{2+}$ -bound state than in the apo state.  $\text{Ca}^{2+}$  binding also appears to restrict the mobility of residues I449 and E452 as is visualized in Fig. 6, with residues presented in red if the quantity  $\Delta S^2 = S_{\text{Ca}^{2+}}^2 - S_{\text{apo}}^2$  is  $>0.05$ .

$\text{Ca}^{2+}$  binding also affects the time scale of motions in the major acidic segment. While the  $\tau_{\text{int}}$  values are  $<20 \text{ ps}$  for most residues in both states, large  $\tau_{\text{int}}$  values, 1048 and 444 ps, are found for residues F450 and E451, respectively, in the apo state. Transverse  $^{15}\text{N}$  chemical shift anisotropy–dipolar cross-correlation rates  $\eta_{xy}$  indicate that neither of these residues exhibits conformational exchange on the microsecond-to-millisecond time scale. Note, however, that fits for both of these residues are susceptible to the effects of structural uncertainty in this region. E451, for example, is one of 13 residues that were excluded from the characterization of the diffusion tensor due to poor RDC agreement with the crystal structure. These residues were fit using a site-specific  $\tau_{\text{loc}}$  value (see Eq. (1) in the Materials and Methods section). F450 was not excluded from the diffusion tensor optimization, but the angle between the F450 N–H bond vector and the unique axis of the diffusion tensor is relatively small ( $\theta = 29.5^\circ$ ). In this case, the fitting parameters are more susceptible to the effects of structural uncertainty, particularly



**Fig. 6.** Structural context for the change in  $S^2$  that accompanies  $\text{Ca}^{2+}$  binding. Residues for which  $\Delta S^2 > 0.05$  are represented in red. The residue for which  $\Delta S^2 < -0.05$  is represented in blue.

in molecules such as CBD1, whose tumbling is highly anisotropic.

Three residues in the proximity of the major acidic segment also exhibit large  $\Delta S^2$  values. They are E385, whose side-chain carboxylate group acts as a  $\text{Ca}^{2+}$ -binding ligand, as well as A416 and S420, which are near the  $\text{Ca}^{2+}$ -binding residue D421. A small number of residues outside the binding loops also exhibit  $\Delta S^2$  values greater than 0.05. In most cases, these long-range effects map to isolated positions in the loops located at the opposite end of the domain. Only a few residues exhibit the opposite trend in  $\Delta S^2$ . Leu483, which is presented in blue in Fig. 6, is the only case where  $\Delta S^2$  is less than  $-0.05$ . Collectively, the order parameters demonstrate that  $\text{Ca}^{2+}$  binding rigidifies the binding site residues and is accompanied by a few (isolated) changes at the opposite end of the molecule.

### $S^2$ comparison with other $\text{Ca}^{2+}$ -binding proteins

The mean order parameter change,  $\Delta S^2 = S_{\text{Ca}^{2+}}^2 - S_{\text{apo}}^2$ , across the major acidic segment (residues 446–454) and other binding site residues (residues 385 and 421) is 0.048. This value is comparable to the changes observed in the  $\text{Ca}^{2+}$ -binding proteins calbindin  $\text{D}_{9\text{k}}$  and the N-domain of cardiac troponin

C (cNTnC), both of which have been extensively studied by  $^{15}\text{N}$  relaxation spectroscopy. The mean  $\Delta S^2$  value of the binding site residues 14–27 and 54–65 of calbindin  $\text{D}_{9\text{k}}$  is 0.047 according to Supplementary Table 4 of Mäler *et al.*<sup>75</sup> Similarly, Table 2 of Spyrapoulos *et al.* yields a mean  $\Delta S^2$  value of 0.034 for binding site residues 29–40 and 65–76 of cNTnC.<sup>42</sup> In order to relate these dynamic changes to changes in actual thermodynamics, it is common to calculate the conformational entropy associated with a given order parameter. The two methods that are most commonly used for this purpose are those by Akke *et al.* and Yang and Kay.<sup>76,77</sup> When applied to the order parameters of the binding site residues, the latter method, which was used in Spyrapoulos *et al.* and Mäler *et al.*, yields  $-T\Delta S$  values of 2.1, 3.4, and 2.7 kcal mol<sup>-1</sup> for CBD1, calbindin  $\text{D}_{9\text{k}}$ , and cNTnC, respectively, which are very similar to the values obtained by the approach of Akke *et al.*<sup>42,75</sup> On a per-residue basis, the relevant values are 0.23, 0.13, and 0.12 kcal mol<sup>-1</sup> residue<sup>-1</sup>. These results indicate that  $\text{Ca}^{2+}$  binding is accompanied by a local decrease in backbone conformational entropy for all three systems. Interestingly, the entropy change per binding-site residue can vary significantly between the different  $\text{Ca}^{2+}$ -binding motifs. The larger entropy change per residue that is obtained for CBD1 originates, in part, from the fact that the average order parameters for CBD1 are slightly higher than those for the other two systems. As a result, the entropy change falls into the steeper portion of the order parameter–entropy relationship.<sup>76,77</sup>

While the comparison between CBD1 and the EF-hand proteins is useful, the difference between CBD1's  $\beta$ -sandwich structure of the  $\text{C}_2$ -domain family and the EF-hand structure must be taken into account. Two of the most extensively studied  $\text{C}_2$  domains are  $\text{C}_2\text{A}$  and  $\text{C}_2\text{B}$ , which are located in tandem as part of a large cytoplasmic segment of the integral membrane protein synaptotagmin I. This arrangement is analogous in many ways to the structural context of CBD1 and CBD2 in the cytoplasmic loop of the NCX. Both  $\text{C}_2\text{A}$  and  $\text{C}_2\text{B}$  exhibit local structural changes in the binding loops in response to  $\text{Ca}^{2+}$ , but neither domain exhibits a large conformational change.<sup>27,78</sup> Future NMR relaxation studies of  $\text{C}_2\text{A}$  and  $\text{C}_2\text{B}$  would provide additional information about the role of dynamics in the binding mechanism of other  $\text{C}_2$  domains. Further studies are also needed in order to characterize the effects of  $\text{Ca}^{2+}$  on the intramolecular interactions between CBD1 and CBD2 in the NCX and between  $\text{C}_2\text{A}$  and  $\text{C}_2\text{B}$  in synaptotagmin I. Of note, a fluorescent resonance energy transfer study of synaptotagmin I indicates that the two  $\text{C}_2$  domains are in closer proximity when  $\text{Ca}^{2+}$  is bound.<sup>79</sup> This finding is consistent with a previously developed model of the NCX that includes an extended interaction interface between CBD1 and CBD2 in the presence of  $\text{Ca}^{2+}$ .<sup>9</sup> Future NMR studies will test this model and determine how the changes identified here in the CBD1-binding site are transmitted to other parts of the molecule.

## Conclusions

The effect of  $\text{Ca}^{2+}$  on the structure and dynamics of CBD1 has been studied by NMR chemical shifts, RDCs, and generalized order parameters at 800 MHz field strength. These quantities provide a highly consistent, site-specific description of the changes that accompany  $\text{Ca}^{2+}$  binding. The data indicate that the two states share common structure and dynamics within the core of the domain. Structural changes at the binding sites, however, are indicated by differences in chemical shifts and RDCs between the two states. Spin relaxation measurements confirm that residues exhibiting a significant conformational change are, in many cases, sites of altered dynamics.  $\text{Ca}^{2+}$  binding restricts the mobility of the major acidic segment and affects the dynamics of other nearby binding loops. Collectively, these findings indicate that the structural and dynamic changes that accompany  $\text{Ca}^{2+}$  binding map predominantly to the binding site residues and their vicinity. In the intact exchanger, the presence of the second  $\text{Ca}^{2+}$ -binding domain CBD2 may induce additional structural and dynamic effects that contribute to the allosteric regulation of the NCX. Such effects will be investigated in future studies of constructs containing both CBD1 and CBD2 using approaches similar to the ones employed here.

## Materials and Methods

### Sample preparation

Canine NCX1 (residues 371–509) was expressed from a pET23b vector in *Escherichia coli* BL21(DE3) cells at 37 °C for 5 h using 0.5 mM IPTG for induction. In addition to the native sequence, the protein contained an eight-residue N-terminal His tag that facilitated purification with a Ni-NTA column (Qiagen). Samples were uniformly  $^{15}\text{N}/^{13}\text{C}$ -labeled for chemical shift assignments of the apo state and for RDC measurements of the  $\text{Ca}^{2+}$ -bound state. All other measurements were performed on uniformly  $^{15}\text{N}$ -labeled protein. NMR samples contained ~0.4 mM protein, 20 mM Hepes (pH 7.0), 20 mM  $\beta$ -mercaptoethanol, and 0.02%  $\text{NaN}_3$  in 90%  $\text{H}_2\text{O}/10\%$   $\text{D}_2\text{O}$ . The  $\text{Ca}^{2+}$ -bound CBD1 samples also contained 20 mM  $\text{CaCl}_2$ . Alternatively, the apo samples contained 15 mM ethylenediaminetetraacetic acid and 100 mM NaCl. Compared to previous studies, it was found that the sample integrity of apo CBD1 was much prolonged under these conditions, in particular for protein concentrations around 0.4 mM. The liquid crystalline medium used for RDC measurements contained 3% C12E5/hexanol at a molar ratio  $r=0.96$ .<sup>60</sup> Sedimentation velocity experiments were performed with a Beckman XL-I ProteomeLab analytical ultracentrifuge equipped with an absorbance optical system. Sample conditions for the sedimentation velocity experiments matched those of the NMR sample conditions, including both protein concentration and temperature. The program SEDFIT<sup>80</sup> was used to determine the sedimentation coefficient distributions, which indicate the presence of a single monomeric species in both states (see Supplementary Materials).

### NMR spectroscopy

Experiments were performed at 306 K on a Bruker 800-MHz spectrometer equipped with a TCI cryoprobe. Chemical shift assignments for the apo state were obtained from HNCO, HN(CA)CO, HNCA, HN(CO)CA, and CBCA (CO)NH spectra.<sup>81</sup> RDCs were obtained from [ $^{15}\text{N},^1\text{H}$ ] HSQC in-phase/antiphase spectra.<sup>82</sup> Longitudinal ( $T_1$ ) and transverse ( $T_2$ ) relaxation times, as well as  $\{^1\text{H}\}$ - $^{15}\text{N}$  steady-state nuclear Overhauser effects, were measured using standard  $^{15}\text{N}$  relaxation methods.<sup>83,84</sup> Transverse  $^{15}\text{N}$  chemical shift anisotropy–dipolar cross-correlation rates ( $\eta_{xy}$ ) were measured using an in-phase/antiphase type spectrum.<sup>85</sup> Spectra were processed by NMRPipe<sup>86</sup> and analyzed with SPARKY (SPARKY 3; T.D. Goddard and D. G. Kneller, University of California, San Francisco, CA).

### Data analysis

RDCs and diffusion tensors were fit using the quadric approach to the crystal structure (2DPK) via singular value decomposition using the MATLAB software.<sup>69,87</sup> The calculation of the alignment tensor was initially performed with all of the available residues. The procedure was then repeated with a subset of residues for which the quantity  $|RDC_{\text{calc}} - RDC_{\text{exp}}| / \text{rms}(RDC_{\text{exp}}) < 0.5$ , where rms is the root mean square function. Relaxation rate constants were obtained by fitting the cross-peak intensities to a single exponential function using the program CurveFit (CurveFit; A.G. Palmer, Columbia University). Duplicate time points provided a measure of the random error in the peak intensities. Monte Carlo simulations were subsequently performed in order to estimate the uncertainty in the rate constants from the measured peak intensity errors. Model-free calculations were performed with the program ModelFree4 (ModelFree; A.G. Palmer, Columbia University.) An initial model-free analysis was performed using the following spectral density function:<sup>40,67,69</sup>

$$J(\omega) = \frac{2}{5} \left[ S^2 \frac{\tau_{\text{loc}}}{1 + (\omega\tau_{\text{loc}})^2} + (1 - S^2) \frac{\tau}{1 + (\omega\tau)^2} \right] \quad (1)$$

$$\tau^{-1} = \tau_{\text{loc}}^{-1} + \tau_{\text{int}}^{-1}$$

where  $S^2$  is the generalized order parameter,  $\tau_{\text{int}}$  is the internal correlation time, and  $\tau_{\text{loc}}$  is the overall correlation time sensed locally by an individual bond vector. Model-free calculations were performed with an N–H bond length of  $r_{\text{NH}} = 1.02$  Å and a chemical shift anisotropy of  $\Delta\sigma = -172$  ppm. Following the initial model-free fit, a set of core residues was selected in order to characterize the rotational diffusion tensor. A residue was included in this set of core residues if all of the following criteria were met. (1) The bond vector orientation was consistent with the  $\text{Ca}^{2+}$ -bound crystal structure. This criterion was met if the quantity  $|RDC_{\text{calc}} - RDC_{\text{exp}}| / \text{rms}(RDC_{\text{exp}}) < 0.5$ . (2) The residue showed no signs of conformational exchange. This criterion was met if the quantity  $\eta_{xy}/R_2 > 0.65$ , where  $R_2 = T_2^{-1}$ . (3) The residue showed no signs of long time-scale internal dynamics in the initial model-free fit with Eq. (1) (i.e., when  $\tau_{\text{int}} < 100$  ps). The model-free analysis was then repeated with this set of core residues using the spectral density function for an axially symmetric diffusion tensor:<sup>67,68</sup>

$$J(\omega) = \frac{2}{5} \sum_{j=0}^2 A_j \left[ S^2 \frac{\tau_j}{1 + (\omega\tau_j)^2} + (1 - S^2) \frac{\tau_j'}{1 + (\omega\tau_j')^2} \right] \quad (2)$$

$$\tau_j' = (\tau_j^{-1} + \tau_{\text{int}}^{-1})^{-1}$$

where  $\tau_j^{-1} = 6D_{\perp} - j^2(D_{\perp} - D_{\parallel})$ ;  $D_{\parallel}$  and  $D_{\perp}$  are the diffusion coefficients;  $A_0 = (3\cos^2\theta - 1)^2/4$ ;  $A_1 = 3\sin^2\theta\cos^2\theta$ ;  $A_2 = (3/4)\sin^4\theta$ ; and  $\theta$  is the angle between the bond vector and the unique axis of the diffusion tensor. The  $\text{Ca}^{2+}$ -bound crystal structure was used as a reference structure, which was rotated into the principal axis frame of the diffusion tensor as part of this procedure. Errors in the model-free parameters were estimated by Monte Carlo analysis. The optimized diffusion tensor was verified for this set of core residues by the quadric method<sup>69,88</sup> using the program quadric\_diffusion (quadric\_diffusion; A.G. Palmer, Columbia University). Residues that met criterion 1, but not criterion 2 or criterion 3, were included in a final round of model-free calculations using the spectral density function in Eq. (2), but with the previously optimized diffusion tensor fixed. In order to account for the effects of conformational exchange,  $R_{\text{ex}}$  terms were included in the fitting procedure for residues that were excluded by criterion 2. Note, however, that residue G399 is the only residue for which a large  $R_{\text{ex}}$  term is observed (10.55 and 10.19  $\text{s}^{-1}$  in the  $\text{Ca}^{2+}$ -bound state and the apo state, respectively). Residues that did not meet criterion 1 or that were absent in the crystal structure due to weak electron density were excluded from the final round of model-free calculations due to their large orientational uncertainty. For these residues, the  $S^2$  and  $\tau_{\text{int}}$  values that are reported correspond to the results originally obtained using the spectral density function in Eq. (1).

## Acknowledgements

We thank Prof. Stephan Grzesiek for providing NMR relaxation pulse programs and Prof. Andrew Herr for performing the analytical ultracentrifugation experiments. Stephan Hilge provided the artwork for Fig. 1a. E.J. is the recipient of a postdoctoral fellowship from the American Heart Association, Greater Southeast Affiliate. S.A.S. is the recipient of a National Institutes of Health postdoctoral fellowship. This work was supported by the Dutch Science Foundation NOW (grant 700.55.443 to G.W.V.) and the National Science Foundation (grant 0621482 to R.B.).

## Supplementary Data

Supplementary data associated with this article can be found, in the online version, at [doi:10.1016/j.jmb.2008.01.046](https://doi.org/10.1016/j.jmb.2008.01.046)

## References

- Berridge, M. J., Bootman, M. D. & Roderick, H. L. (2003). Calcium signalling: dynamics, homeostasis and remodelling. *Nat. Rev. Mol. Cell Biol.* **4**, 517–529.
- Carafoli, E. (2002). Calcium signaling: a tale for all seasons. *Proc. Natl Acad. Sci. USA*, **99**, 1115–1122.
- Sipido, K. R., Volders, P. G., Vos, M. A. & Verdonck, F. (2002). Altered  $\text{Na}^+/\text{Ca}^{2+}$  exchange activity in cardiac hypertrophy and heart failure: a new target for therapy? *Cardiovasc. Res.* **53**, 782–805.
- Philipson, K. D. & Nicoll, D. A. (2000). Sodium-calcium exchange: a molecular perspective. *Annu. Rev. Physiol.* **62**, 111–133.
- Reuter, H., Pott, C., Goldhaber, J. I., Henderson, S. A., Philipson, K. D. & Schwinger, R. H. (2005).  $\text{Na}^+-\text{Ca}^{2+}$  exchange in the regulation of cardiac excitation-contraction coupling. *Cardiovasc. Res.* **67**, 198–207.
- Kang, T. M. & Hilgemann, D. W. (2004). Multiple transport modes of the cardiac  $\text{Na}^+/\text{Ca}^{2+}$  exchanger. *Nature*, **427**, 544–548.
- Iwamoto, T., Nakamura, T. Y., Pan, Y., Uehara, A., Imanaga, I. & Shigekawa, M. (1999). Unique topology of the internal repeats in the cardiac  $\text{Na}^+/\text{Ca}^{2+}$  exchanger. *FEBS Lett.* **446**, 264–268.
- Nicoll, D. A., Ottolia, M., Lu, L., Lu, Y. & Philipson, K. D. (1999). A new topological model of the cardiac sarcolemmal  $\text{Na}^+-\text{Ca}^{2+}$  exchanger. *J. Biol. Chem.* **274**, 910–917.
- Hilge, M., Aelen, J. & Vuister, G. W. (2006).  $\text{Ca}^{2+}$  regulation in the  $\text{Na}^+/\text{Ca}^{2+}$  exchanger involves two markedly different  $\text{Ca}^{2+}$  sensors. *Mol. Cell*, **22**, 15–25.
- Pettersen, E. F., Goddard, T. D., Huang, C. C., Couch, G. S., Greenblatt, D. M., Meng, E. C. & Ferrin, T. E. (2004). UCSF Chimera: a visualization system for exploratory research and analysis. *J. Comput. Chem.* **25**, 1605–1612.
- Nicoll, D. A., Sawaya, M. R., Kwon, S., Cascio, D., Philipson, K. D. & Abramson, J. (2006). The crystal structure of the primary  $\text{Ca}^{2+}$  sensor of the  $\text{Na}^+/\text{Ca}^{2+}$  exchanger reveals a novel  $\text{Ca}^{2+}$  binding motif. *J. Biol. Chem.* **281**, 21577–21581.
- Ottolia, M., Philipson, K. D. & John, S. (2004). Conformational changes of the  $\text{Ca}^{2+}$  regulatory site of the  $\text{Na}^+-\text{Ca}^{2+}$  exchanger detected by FRET. *Biophys. J.* **87**, 899–906.
- Chazin, W. J. (1995). Releasing the calcium trigger. *Nat. Struct. Biol.* **2**, 707–710.
- Kördel, J., Skelton, N. J., Akke, M. & Chazin, W. J. (1993). High-resolution structure of calcium-loaded calbindin  $\text{D}_{9k}$ . *J. Mol. Biol.* **231**, 711–734.
- Skelton, N. J., Kördel, J. & Chazin, W. J. (1995). Determination of the solution structure of apo calbindin  $\text{D}_{9k}$  by NMR spectroscopy. *J. Mol. Biol.* **249**, 441–462.
- Chou, J. J., Li, S., Klee, C. B. & Bax, A. (2001). Solution structure of  $\text{Ca}^{2+}$ -calmodulin reveals flexible hand-like properties of its domains. *Nat. Struct. Biol.* **8**, 990–997.
- Kuboniwa, H., Tjandra, N., Grzesiek, S., Ren, H., Klee, C. B. & Bax, A. (1995). Solution structure of calcium-free calmodulin. *Nat. Struct. Biol.* **2**, 768–776.
- Zhang, M., Tanaka, T. & Ikura, M. (1995). Calcium-induced conformational transition revealed by the solution structure of apo calmodulin. *Nat. Struct. Biol.* **2**, 758–767.
- Blanchard, H., Grochulski, P., Li, Y., Arthur, J. S., Davies, P. L., Elce, J. S. & Cygler, M. (1997). Structure of a calpain  $\text{Ca}^{2+}$ -binding domain reveals a novel EF-hand and  $\text{Ca}^{2+}$ -induced conformational changes. *Nat. Struct. Biol.* **4**, 532–538.
- Ames, J. B., Ishima, R., Tanaka, T., Gordon, J. I., Stryer, L. & Ikura, M. (1997). Molecular mechanics of calcium-myristoyl switches. *Nature*, **389**, 198–202.
- Tanaka, T., Ames, J. B., Harvey, T. S., Stryer, L. & Ikura, M. (1995). Sequestration of the membrane-targeting myristoyl group of recoverin in the calcium-free state. *Nature*, **376**, 444–447.
- Wingard, J. N., Chan, J., Bosanac, I., Haeseleer, F., Palczewski, K., Ikura, M. & Ames, J. B. (2005). Structural analysis of  $\text{Mg}^{2+}$  and  $\text{Ca}^{2+}$  binding to CaBP1, a neuron-specific regulator of calcium channels. *J. Biol. Chem.* **280**, 37461–37470.

23. Findlay, W. A., Sonnichsen, F. D. & Sykes, B. D. (1994). Solution structure of the TR1C fragment of skeletal muscle troponin-C. *J. Biol. Chem.* **269**, 6773–6778.
24. Gagné, S. M., Tsuda, S., Li, M. X., Smillie, L. B. & Sykes, B. D. (1995). Structures of the troponin C regulatory domains in the apo and calcium-saturated states. *Nat. Struct. Biol.* **2**, 784–789.
25. Sia, S. K., Li, M. X., Spyrapopoulos, L., Gagné, S. M., Liu, W., Putkey, J. A. & Sykes, B. D. (1997). Structure of cardiac muscle troponin C unexpectedly reveals a closed regulatory domain. *J. Biol. Chem.* **272**, 18216–18221.
26. Spyrapopoulos, L., Li, M. X., Sia, S. K., Gagné, S. M., Chandra, M., Solaro, R. J. & Sykes, B. D. (1997). Calcium-induced structural transition in the regulatory domain of human cardiac troponin C. *Biochemistry*, **36**, 12138–12146.
27. Shao, X., Fernandez, I., Südhof, T. C. & Rizo, J. (1998). Solution structures of the  $\text{Ca}^{2+}$ -free and  $\text{Ca}^{2+}$ -bound C2A domain of synaptotagmin I: does  $\text{Ca}^{2+}$  induce a conformational change? *Biochemistry*, **37**, 16106–16115.
28. Cheng, Y., Sequeira, S. M., Malinina, L., Tereshko, V., Sollner, T. H. & Patel, D. J. (2004). Crystallographic identification of  $\text{Ca}^{2+}$  and  $\text{Sr}^{2+}$  coordination sites in synaptotagmin I C2B domain. *Protein Sci.* **13**, 2665–2672.
29. Bertini, I., Del Bianco, C., Gelis, I., Katsaros, N., Luchinat, C., Parigi, G. *et al.* (2004). Experimentally exploring the conformational space sampled by domain reorientation in calmodulin. *Proc. Natl Acad. Sci. USA*, **101**, 6841–6846.
30. Bertini, I., Gupta, Y. K., Luchinat, C., Parigi, G., Peana, M., Sgheri, L. & Yuan, J. (2007). Paramagnetism-based NMR restraints provide maximum allowed probabilities for the different conformations of partially independent protein domains. *J. Am. Chem. Soc.* **129**, 12786–12794.
31. Brüschweiler, R. (2003). New approaches to the dynamic interpretation and prediction of NMR relaxation data from proteins. *Curr. Opin. Struct. Biol.* **13**, 175–183.
32. Palmer, A. G., 3rd (2004). NMR characterization of the dynamics of biomacromolecules. *Chem. Rev.* **104**, 3623–3640.
33. Jarymowycz, V. A. & Stone, M. J. (2006). Fast time scale dynamics of protein backbones: NMR relaxation methods, applications, and functional consequences. *Chem. Rev.* **106**, 1624–1671.
34. Akke, M., Skelton, N. J., Kördel, J., Palmer, A. G., 3rd & Chazin, W. J. (1993). Effects of ion binding on the backbone dynamics of calbindin  $\text{D}_{9k}$  determined by  $^{15}\text{N}$  NMR relaxation. *Biochemistry*, **32**, 9832–9844.
35. Evenäs, J., Forsén, S., Malmendal, A. & Akke, M. (1999). Backbone dynamics and energetics of a calmodulin domain mutant exchanging between closed and open conformations. *J. Mol. Biol.* **289**, 603–617.
36. Kördel, J., Skelton, N. J., Akke, M., Palmer, A. G., 3rd & Chazin, W. J. (1992). Backbone dynamics of calcium-loaded calbindin  $\text{D}_{9k}$  studied by two-dimensional proton-detected  $^{15}\text{N}$  NMR spectroscopy. *Biochemistry*, **31**, 4856–4866.
37. Malmendal, A., Carlström, G., Hambræus, C., Drakenberg, T., Forsén, S. & Akke, M. (1998). Sequence and context dependence of EF-hand loop dynamics. An  $^{15}\text{N}$  relaxation study of a calcium-binding site mutant of calbindin  $\text{D}_{9k}$ . *Biochemistry*, **37**, 2586–2595.
38. Malmendal, A., Evenäs, J., Forsén, S. & Akke, M. (1999). Structural dynamics in the C-terminal domain of calmodulin at low calcium levels. *J. Mol. Biol.* **293**, 883–899.
39. Malmendal, A., Vander Kooi, C. W., Nielsen, N. C. & Chazin, W. J. (2005). Calcium-modulated S100 protein-phospholipid interactions. An NMR study of calbindin  $\text{D}_{9k}$  and DPC. *Biochemistry*, **44**, 6502–6512.
40. Barbato, G., Ikura, M., Kay, L. E., Pastor, R. W. & Bax, A. (1992). Backbone dynamics of calmodulin studied by  $^{15}\text{N}$  relaxation using inverse detected two-dimensional NMR spectroscopy: the central helix is flexible. *Biochemistry*, **31**, 5269–5278.
41. Gagné, S. M., Tsuda, S., Spyrapopoulos, L., Kay, L. E. & Sykes, B. D. (1998). Backbone and methyl dynamics of the regulatory domain of troponin C: anisotropic rotational diffusion and contribution of conformational entropy to calcium affinity. *J. Mol. Biol.* **278**, 667–686.
42. Spyrapopoulos, L., Gagné, S. M., Li, M. X. & Sykes, B. D. (1998). Dynamics and thermodynamics of the regulatory domain of human cardiac troponin C in the apo- and calcium-saturated states. *Biochemistry*, **37**, 18032–18044.
43. Spyrapopoulos, L., Lavigne, P., Crump, M. P., Gagné, S. M., Kay, C. M. & Sykes, B. D. (2001). Temperature dependence of dynamics and thermodynamics of the regulatory domain of human cardiac troponin C. *Biochemistry*, **40**, 12541–12551.
44. Smalridge, R. S., Whiteman, P., Werner, J. M., Campbell, I. D., Handford, P. A. & Downing, A. K. (2003). Solution structure and dynamics of a calcium binding epidermal growth factor-like domain pair from the neonatal region of human fibrillin-1. *J. Biol. Chem.* **278**, 12199–12206.
45. Werner, J. M., Knott, V., Handford, P. A., Campbell, I. D. & Downing, A. K. (2000). Backbone dynamics of a cbEGF domain pair in the presence of calcium. *J. Mol. Biol.* **296**, 1065–1078.
46. Yuan, X., Werner, J. M., Lack, J., Knott, V., Handford, P. A., Campbell, I. D. & Downing, A. K. (2002). Effects of the N2144S mutation on backbone dynamics of a TB-cbEGF domain pair from human fibrillin-1. *J. Mol. Biol.* **316**, 113–125.
47. Häussinger, D., Ahrens, T., Sass, H. J., Pertz, O., Engel, J. & Grzesiek, S. (2002). Calcium-dependent homo-association of E-cadherin by NMR spectroscopy: changes in mobility, conformation and mapping of contact regions. *J. Mol. Biol.* **324**, 823–839.
48. Babini, E., Bertini, I., Capozzi, F., Chirivino, E. & Luchinat, C. (2006). A structural and dynamic characterization of the EF-hand protein CLSP. *Structure*, **14**, 1029–1038.
49. Capozzi, F., Casadei, F. & Luchinat, C. (2006). EF-hand protein dynamics and evolution of calcium signal transduction: an NMR view. *J. Biol. Inorg. Chem.* **11**, 949–962.
50. Ikura, M. & Ames, J. B. (2006). Genetic polymorphism and protein conformational plasticity in the calmodulin superfamily: two ways to promote multifunctionality. *Proc. Natl Acad. Sci. USA*, **103**, 1159–1164.
51. Bhattacharya, S., Bunick, C. G. & Chazin, W. J. (2004). Target selectivity in EF-hand calcium binding proteins. *Biochim. Biophys. Acta*, **1742**, 69–79.
52. Grabarek, Z. (2006). Structural basis for diversity of the EF-hand calcium-binding proteins. *J. Mol. Biol.* **359**, 509–525.
53. Rizo, J. & Südhof, T. C. (1998). C2-domains, structure and function of a universal  $\text{Ca}^{2+}$ -binding domain. *J. Biol. Chem.* **273**, 15879–15882.
54. Nalefski, E. A. & Falke, J. J. (1996). The C2 domain calcium-binding motif: structural and functional diversity. *Protein Sci.* **5**, 2375–2390.
55. Chapman, E. R. (2002). Synaptotagmin: a  $\text{Ca}^{2+}$  sensor that triggers exocytosis? *Nat. Rev. Mol. Cell Biol.* **3**, 498–508.

56. Xu, G. Y., McDonagh, T., Yu, H. A., Nalefski, E. A., Clark, J. D. & Cumming, D. A. (1998). Solution structure and membrane interactions of the C2 domain of cytosolic phospholipase A2. *J. Mol. Biol.* **280**, 485–500.
57. Shao, X., Davletov, B. A., Sutton, R. B., Südhof, T. C. & Rizo, J. (1996). Bipartite Ca<sup>2+</sup>-binding motif in C2 domains of synaptotagmin and protein kinase C. *Science*, **273**, 248–251.
58. Essen, L. O., Perisic, O., Cheung, R., Katan, M. & Williams, R. L. (1996). Crystal structure of a mammalian phosphoinositide-specific phospholipase C delta. *Nature*, **380**, 595–602.
59. Biekofsky, R. R., Martin, S. R., Browne, J. P., Bayley, P. M. & Feeney, J. (1998). Ca<sup>2+</sup> coordination to backbone carbonyl oxygen atoms in calmodulin and other EF-hand proteins: <sup>15</sup>N chemical shifts as probes for monitoring individual-site Ca<sup>2+</sup> coordination. *Biochemistry*, **37**, 7617–7629.
60. Rückert, M. & Otting, G. (2000). Alignment of biological macromolecules in novel nonionic liquid crystalline media for NMR experiments. *J. Am. Chem. Soc.* **122**, 7793–7797.
61. Bax, A. (2003). Weak alignment offers new NMR opportunities to study protein structure and dynamics. *Protein Sci.* **12**, 1–16.
62. Tolman, J. R. & Ruan, K. (2006). NMR residual dipolar couplings as probes of biomolecular dynamics. *Chem. Rev.* **106**, 1720–1736.
63. Blackledge, M. (2005). Recent progress in the study of biomolecular structure and dynamics in solution from residual dipolar couplings. *Prog. Nucl. Magn. Reson. Spectrosc.* **46**, 23–61.
64. Prestegard, J. H., Bougault, C. M. & Kishore, A. I. (2004). Residual dipolar couplings in structure determination of biomolecules. *Chem. Rev.* **104**, 3519–3540.
65. Clore, G. M. & Schwieters, C. D. (2002). Theoretical and computational advances in biomolecular NMR spectroscopy. *Curr. Opin. Struct. Biol.* **12**, 146–153.
66. Meiler, J., Prompers, J. J., Peti, W., Griesinger, C. & Brüschweiler, R. (2001). Model-free approach to the dynamic interpretation of residual dipolar couplings in globular proteins. *J. Am. Chem. Soc.* **123**, 6098–6107.
67. Lipari, G. & Szabo, A. (1982). Model-free approach to the interpretation of nuclear magnetic resonance relaxation in macromolecules: 1. Theory and range of validity. *J. Am. Chem. Soc.* **104**, 4546–4559.
68. Woessner, D. E. (1962). Nuclear spin relaxation in ellipsoids undergoing rotational Brownian motion. *J. Chem. Phys.* **37**, 647.
69. Brüschweiler, R., Liao, X. & Wright, P. E. (1995). Long-range motional restrictions in a multidomain zinc-finger protein from anisotropic tumbling. *Science*, **268**, 886–889.
70. Andrec, M., Inman, K. G., Weber, D. J., Levy, R. M. & Montelione, G. T. (2000). A Bayesian statistical method for the detection and quantification of rotational diffusion anisotropy from NMR relaxation data. *J. Magn. Reson.* **146**, 66–80.
71. Carr, P. A., Erickson, H. P. & Palmer, A. G., 3rd (1997). Backbone dynamics of homologous fibronectin type III cell adhesion domains from fibronectin and tennascin. *Structure*, **5**, 949–959.
72. Siggers, K., Soto, C. & Palmer, A. G., 3rd (2007). Conformational dynamics in loop swap mutants of homologous fibronectin Type III domains. *Biophys. J.* **93**, 2447–2456.
73. Halaby, D. M., Poupon, A. & Mornon, J. (1999). The immunoglobulin fold family: sequence analysis and 3D structure comparisons. *Protein Eng.* **12**, 563–571.
74. Richardson, J. S. & Richardson, D. C. (2002). Natural beta-sheet proteins use negative design to avoid edge-to-edge aggregation. *Proc. Natl Acad. Sci. USA*, **99**, 2754–2759.
75. Mäler, L., Blankenship, J., Rance, M. & Chazin, W. J. (2000). Site-site communication in the EF-hand Ca<sup>2+</sup>-binding protein calbindin D<sub>9k</sub>. *Nat. Struct. Biol.* **7**, 245–250.
76. Akke, M., Brüschweiler, R. & Palmer, A. G. (1993). NMR order parameters and free energy: an analytical approach and its application to cooperative Ca<sup>2+</sup> binding by calbindin D<sub>9k</sub>. *J. Am. Chem. Soc.* **115**, 9832–9833.
77. Yang, D. & Kay, L. E. (1996). Contributions to conformational entropy arising from bond vector fluctuations measured from NMR-derived order parameters application to protein folding. *J. Mol. Biol.* **263**, 369–382.
78. Fernandez, I., Araç, D., Ubach, J., Gerber, S. H., Shin, O., Gao, Y. *et al.* (2001). Three-dimensional structure of the synaptotagmin 1 C2B-domain: synaptotagmin 1 as a phospholipid binding machine. *Neuron*, **32**, 1057–1069.
79. García, R. A., Forde, C. E. & Godwin, H. A. (2000). Calcium triggers an intramolecular association of the C2 domains in synaptotagmin. *Proc. Natl Acad. Sci. USA*, **97**, 5883–5888.
80. Schuck, P. (2000). Size-distribution analysis of macromolecules by sedimentation velocity ultracentrifugation and Lamm equation modeling. *Biophys. J.* **78**, 1606–1619.
81. Kanelis, V., Forman-Kay, J. D. & Kay, L. E. (2001). Multidimensional NMR methods for protein structure determination. *IUBMB Life*, **52**, 291–302.
82. Ottiger, M., Delaglio, F. & Bax, A. (1998). Measurement of *J* and dipolar couplings from simplified two-dimensional NMR spectra. *J. Magn. Reson.* **131**, 373–378.
83. Brutscher, B., Brüschweiler, R. & Ernst, R. R. (1997). Backbone dynamics and structural characterization of the partially folded A state of ubiquitin by <sup>1</sup>H, <sup>13</sup>C, and <sup>15</sup>N nuclear magnetic resonance spectroscopy. *Biochemistry*, **36**, 13043–13053.
84. Massi, F., Johnson, E., Wang, C., Rance, M. & Palmer, A. G., 3rd (2004). NMR R1ρ rotating-frame relaxation with weak radio frequency fields. *J. Am. Chem. Soc.* **126**, 2247–2256.
85. Hall, J. B. & Fushman, D. (2003). Direct measurement of the transverse and longitudinal <sup>15</sup>N chemical shift anisotropy-dipolar cross-correlation rate constants using <sup>1</sup>H-coupled HSQC spectra. *Magn. Reson. Chem.* **41**, 837–842.
86. Delaglio, F., Grzesiek, S., Vuister, G. W., Zhu, G., Pfeifer, J. & Bax, A. (1995). NMRPipe: a multidimensional spectral processing system based on UNIX pipes. *J. Biomol. NMR*, **6**, 277–293.
87. Losonczi, J. A., Andrec, M., Fischer, M. W. & Prestegard, J. H. (1999). Order matrix analysis of residual dipolar couplings using singular value decomposition. *J. Magn. Reson.* **138**, 334–342.
88. Lee, L. K., Rance, M., Chazin, W. J. & Palmer, A. G., 3rd (1997). Rotational diffusion anisotropy of proteins from simultaneous analysis of <sup>15</sup>N and <sup>13</sup>C alpha nuclear spin relaxation. *J. Biomol. NMR*, **9**, 287–298.